

DATA-DRIVEN TURBULENCE MODELING FOR MULTI-MECHANISM SEPARATED FLOWS OVER ICED AIRFOILS

Zizhou He[1] and Yufei Zhang[1,2,3]

[1] School of Aerospace Engineering, Tsinghua University, 100084, Beijing, China
[2] State Key Laboratory of Advanced Space Propulsion, Tsinghua University, 100084, Beijing, China
[3] Caofeidian Laboratory, 063200 Tangshan, China

Abstract

Accurate iced wing aerodynamic prediction is hindered by the "dual error mechanism" in RANS models, where eddy viscosity is overestimated upstream and underestimated downstream in separated shear layers. This study proposes the field inversion and physics-driven-classification modeling (FI-PDCM) framework to decouple these opposing error modes. A correction factor β is first determined via discrete adjoint-based field inversion, followed by the formulation of an explicit algebraic model using local features. Validation on the GLC305-944 iced airfoil benchmark demonstrates that the corrected model accurately replicates the β distribution derived from field inversion, capturing the separation bubble physics, surface pressure, and the entire lift curve through stall. Furthermore, tests on a zero-pressure-gradient flat-plate flow confirm that the model effectively deactivates in attached regions, preserving the original predictive accuracy for canonical wall-bounded flows. Future research will focus on testing the model's generalizability across a broader range of ice shapes to further establish its robustness and engineering utility.

Keywords: Data-driven turbulence modeling, Discrete adjoint, Field inversion, Iced wing

1. Introduction

Accurate prediction of iced wing aerodynamics is vital for flight safety but challenging for traditional Reynolds-averaged Navier–Stokes (RANS) models. While computationally efficient, models like Spalart–Allmaras (SA) struggle to capture separated shear layers, leading to substantial errors in lift, drag, and stall prediction. Advancements in field inversion and machine learning (FIML) [1] have enabled data-driven corrections by introducing a correction factor β into the source terms of the turbulence transport equations—specifically targeting the production term in the SA model or the destruction term in the ω-equation for SST $k-\omega$ model. While this technique offers a pathway to higher accuracy, the required values of β often vary drastically depending on both geometric configurations and the underlying flow physics.

Recent literature highlights this conflict of "opposing requirements" for turbulence correction. For instance, in the context of trailing-edge separation and stall prediction, research by He et al. [2] has demonstrated that a reduction in β ($\beta < 1$) is necessary to suppress eddy viscosity on the suction side, thereby allowing the model to capture premature separation. Conversely, for cases such as the NASA hump, Wu et al. [3] found that β must be increased ($\beta > 1$) to enhance eddy viscosity within the shear layer to correctly predict the reattachment point. Duraisamy et al. [4] have further underscored that such divergent correction requirements are not anomalies but a fundamental necessity across varying flow configurations.

This challenge is even more pronounced in iced airfoil flows, where the β correction field often exhibits high spatial heterogeneity within a single flow field. As noted by Yan et al. [5] and Xiao et al. [6], iced airfoils typically suffer from a "dual error mechanism". Specifically, RANS models typically assume fully turbulent flow, leading to an overestimation of eddy viscosity ν_t in the upstream portion

of the shear layer where turbulence is not yet fully developed. Conversely, as turbulent fluctuations intensify downstream, these models often underestimate ν_t, failing to capture the reattachment point. Such spatial heterogeneity necessitates that the correction factor β switch between suppression ($\beta < 1$) and amplification ($\beta > 1$) within a single flow field.

To address these conflicting requirements, this study introduces the field inversion and physics-driven-classification modeling (FI-PDCM) framework. In this approach, the spatial distribution of β is first determined via discrete adjoint-based field inversion. The core innovation then lies in the subsequent modeling stage, where a physical classification strategy is incorporated to decouple these distinct error modes based on local flow features. In this study, an initial version of the data-driven model is constructed based on the SA turbulence model. Preliminary results demonstrate that the FI-PDCM framework significantly improves C_L, C_D, and C_P predictions, particularly for the linear range and stall angle. Future work will validate the model's generalizability across diverse ice shapes.

2. Methodologies

2.1 Field Inversion

The SA model proposed by Spalart et al. [7] is given as follows:

$$\frac{\mathrm{D}\tilde{\nu}}{\mathrm{D}t} = \beta(\boldsymbol{x}) \cdot P - D + \frac{1}{\sigma}\left[\nabla \cdot ((\nu + \tilde{\nu})\nabla\tilde{\nu}) + C_{b2}(\nabla\tilde{\nu})^2\right], \qquad (1)$$

where $\beta(\boldsymbol{x})$ is the correction factor for the production term proposed by Singh et al. [1], used to adjust the magnitude of eddy viscosity at different spatial locations.

The process of adjusting the spatial distribution of β within a given flow field to minimize the discrepancy between CFD results and high-fidelity data (e.g., experiment or DNS) is referred to as field inversion. This process is essentially formulated as the following optimization problem:

$$\min_{\beta} J = \sum_i \lambda_{\mathrm{obs},i}(d_i - h_i(\boldsymbol{\beta}))^2 + \sum_j \lambda_{\mathrm{prior},j}(\beta_j - 1)^2, \quad (2)$$

where d represents the high-fidelity data, and h denotes the CFD results obtained after $\boldsymbol{\beta}$ correction. The first term on the right-hand side quantifies the error of the current CFD predictions, while the second term serves as a regularization term to ensure a smooth β field and prevent overfitting to experimental noise. Terms λ_{obs} and λ_{prior} are weighting coefficients, that can be adjusted to balance the relative influence of the QOI and the prior distribution. To efficiently handle the high-dimensional optimization of the spatial β distribution, the discrete adjoint method [8] is employed for its ability to decouple gradient evaluation costs from the total number of design variables. The implementation details of the discrete adjoint method are documented in Ref. [9]. In this study, both CFD computations and discrete adjoint solutions are performed using a custom-developed version of the open-source solver ADflow [10].

2.2 Model Construction

Once the spatial distribution of β is obtained via field inversion, a mapping between β and local flow features must be established to construct a correction model with generalizability. To ensure the model satisfies physical constraints such as Galilean invariance and locality, a set of candidate training features is constructed based on dimensional analysis and the underlying physical mechanisms of separated flows. The candidate local features are as follows:

$$x_0=\frac{\tilde{\nu}}{\nu}=\chi,\quad x_1=\log\left(\frac{\tau}{\tau_{ref}}+\varepsilon\right),\quad x_2=\log\left(\frac{P}{D+\varepsilon}+\varepsilon\right),\quad x_3=\log\left(\frac{|\nabla\nu|d}{\nu+\nu}+\varepsilon\right),$$
$$x_4=\frac{|\mathbf{\Omega}|}{|\mathbf{S}|},\qquad x_5=tr\left(\mathbf{S}^2\right)=\lambda_1,\qquad x_6=tr\left(\mathbf{\Omega}^2\right)=\lambda_2,\qquad x_7=tr\left(\mathbf{\Omega}^2\cdot\mathbf{S}^2\right)=\lambda_5, \tag{3}$$
$$x_8=|\mathbf{\Omega}|,\qquad x_9=\frac{|\mathbf{\Omega}|d^2}{\nu}=Re_\Omega,\qquad x_{10}=\frac{\sqrt{k}\cdot d}{\nu}=Re_k.$$

For the sake of brevity, the definitions of $x_{0\sim8}$ are omitted here and can be found in Ref. [2]. In Eq. (3), x_9 and x_{10} represent the vorticity-based and turbulent-kinetic-energy-based Reynolds numbers, respectively. Within the SA model framework, the TKE is defined as follows [11]:

$$k=\frac{\mu_t\sqrt{2S_{ij}S_{ij}}}{0.31\rho}. \tag{4}$$

Traditional FIML model construction typically involves fitting a model to a static dataset derived from field inversion. However, this often results in models that perform well on training data but exhibit poor convergence or accuracy when integrated back into CFD solvers. As noted by Holland et al. [12] , training models within the CFD iteration loop is a more effective strategy for ensuring robust performance in practical applications.

In light of this, the present study adopts a CFD-in-loop approach to construct a symbolic-expression-based correction model. The implementation workflow, termed the FI-PDCM framework, is as follows: First, the spatial distribution of the correction factor β and its corresponding features are obtained via discrete adjoint-based field inversion. Second, the β field is categorized based on the underlying physical mechanisms characteristic of the correction regions. Finally, specific algebraic model structures are determined for each region, with their coefficients calibrated using a Genetic Algorithm (GA) [13]. This optimization process is executed using our in-house software SAMO [14], where the objective function is defined by the accuracy of the aerodynamic performance predictions. This integrated framework yields a physics-driven, symbolic correction model specifically tailored for complex separated flows.

3. Model Development

3.1 Field Inversion on the GLC305-944 Iced Airfoil

The GLC305-944 iced airfoil is a widely recognized benchmark used to evaluate the capability of CFD solvers in predicting iced flows. The baseline SA model typically fails to capture the post-ice separation bubble on the suction side, resulting in inaccurate lift coefficient curves and stall angle predictions. In this study, field inversion is performed for this case at $Ma=0.12$ and $Re=3.5\times10^6$ for angles of attack of $4.14°$ and $6.17°$. The objective function is defined as the sum of squared discrepancies between the computed C_L and C_D and the experimental data [15], as formulated in Eq. (5). Specifically, the weighting coefficient for the regularization term is set to 1×10^{-7} to ensure the spatial smoothness of the inverted β field.

$$\min_{\beta} J=(C_{L,\mathrm{Exp}}-C_{L,\mathrm{prid}}(\boldsymbol{\beta}))^2+(C_{D,\mathrm{Exp}}-C_{D,\mathrm{prid}}(\boldsymbol{\beta}))^2+\sum_j(\beta_j-1)^2\times10^{-7}. \tag{5}$$

The optimization process for the objective function during field inversion is illustrated in Figure 1. For both investigated flow conditions, the objective function decreases rapidly and reaches convergence within a few dozen iterations, indicating that the adjoint-based inversion effectively calibrates the SA model's source term. Consequently, the predictive accuracy for aerodynamic coefficients is remarkably enhanced: the computed C_L at $\alpha=4.14°$ improves from a baseline value of 0.385 to 0.487 (matching well with the experimental value of 0.489), while at $\alpha=6.17°$, the C_L increases from 0.471 to 0.668, nearly recovering the experimental measurement of 0.669.

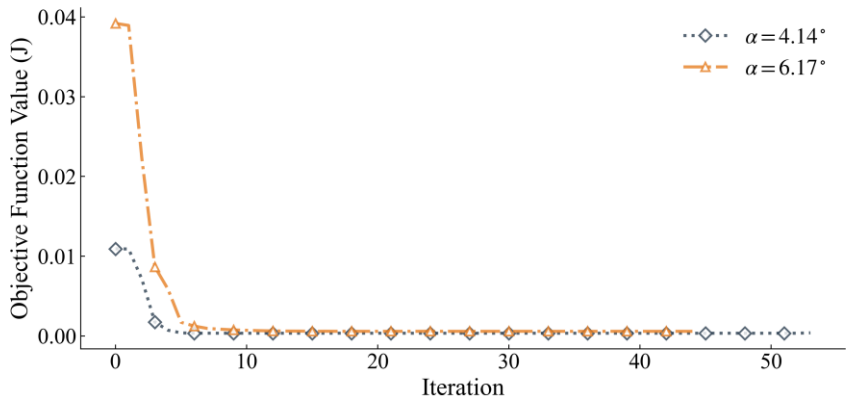
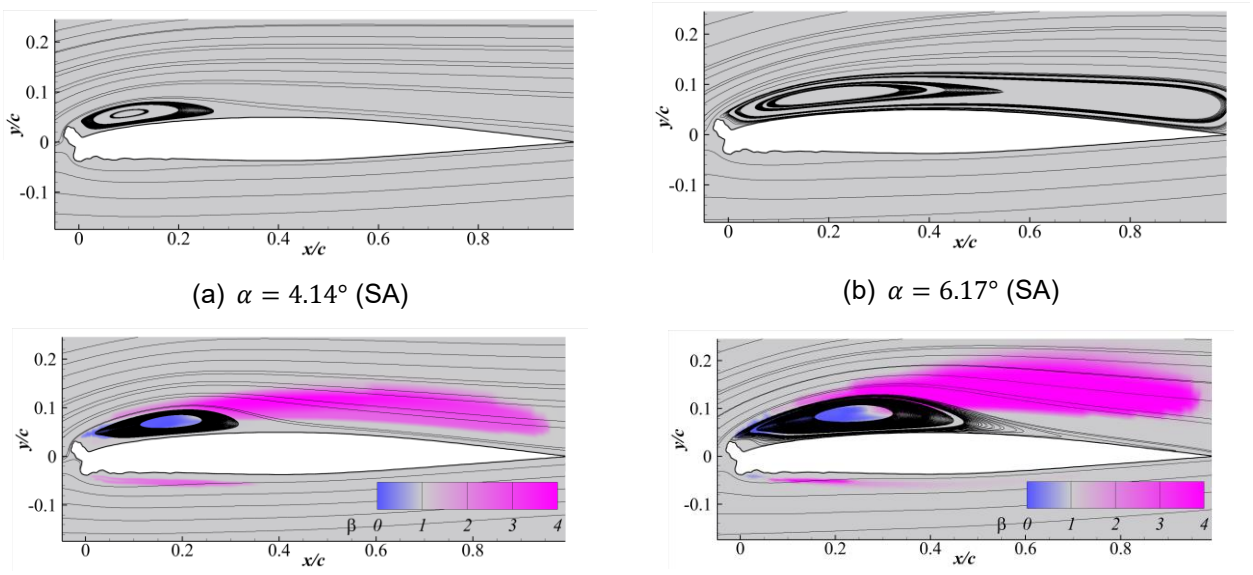


Figure 1 – Iteration history of the objective function value.

To further elucidate the physical mechanism behind these integrated aerodynamic improvements, Figure 2 compares the detailed flow fields predicted by the baseline SA model and the field inversion results. The spatial distribution of β reveals a clear two-stage correction mechanism: it suppresses the production of eddy viscosity in the upstream region of the separated shear layer ($\beta < 1$) while significantly enhancing it further downstream ($\beta > 1$). This specific distribution directly addresses the inherent physical limitations of the standard SA model, which tends to trigger premature turbulence development near the separation point and underpredict turbulent fluctuations as the shear layer evolves. Through the spatially-resolved inversion of the β field, the field inversion successfully rectifies the morphology of the post-ice separation bubble, providing a more physical reconstruction of the separation and reattachment characteristics.



(a) $\alpha = 4.14°$ (SA)

(b) $\alpha = 6.17°$ (SA)

(c) $\alpha = 4.14°$ (FI)

(d) $\alpha = 6.17°$ (FI)

Figure 2 – Comparison of the corrected and baseline flow fields.

3.2 Physics-Driven Feature Analysis and CFD-in-Loop Model Construction

To effectively establish an explicit algebraic model relating β to local flow features, it is first necessary to identify features capable of distinguishing between corrected ($\beta \neq 1$) and uncorrected ($\beta = 1$) regions. As extensively discussed by Li et al. [16], turbulence model corrections for iced airfoil flows primarily target the separated shear layer. Consequently, the vorticity-based Reynolds number Re_Ω is employed to identify and isolate this specific region from the rest of the flow field.

To further classify the regions of suppressed ($\beta < 1$) versus amplified ($\beta > 1$) production within the shear layer, it is essential to distinguish between its upstream and downstream portions. While

traditional modeling typically relies on non-local transition models for this task, the present study adopts a data-driven approach, utilizing correlation analysis to identify discriminative local features. Our analysis of the sub-dataset where $\beta \leq 1$ reveals that the correlations of Re_Ω and Re_k with β reach -0.55 and -0.51, respectively, as illustrated in the correlation heatmap (Figure 3). These values are significantly higher than those of other candidate local features in Eq. (3). Since Re_Ω has already been utilized to trigger the correction region, Re_k and a linear combination of Re_k and Re_Ω are strategically selected as the key features to differentiate the upstream and downstream sections of the shear layer.

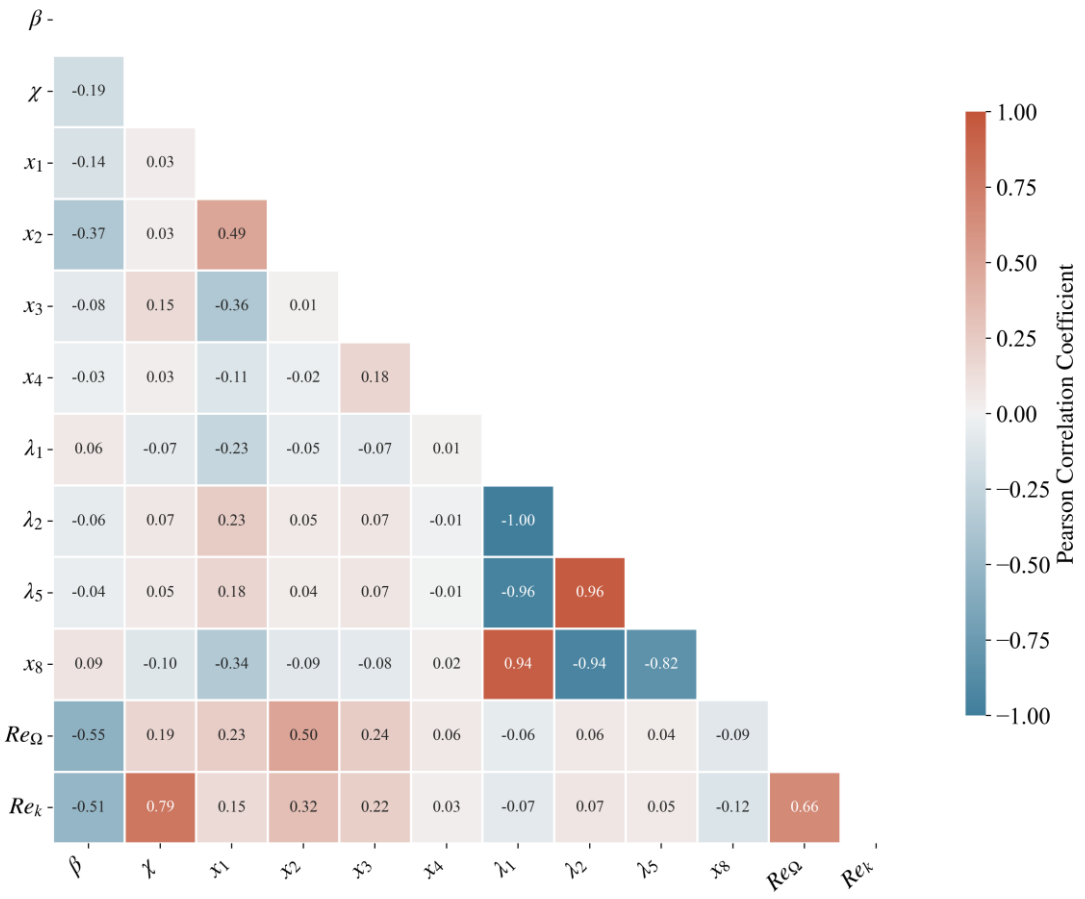


Figure 3 - Correlation of the correction factor β with the features.

Based on the observed characteristics of the β distribution—specifically its boundedness, its adherence to unity across the majority of the flow field, and its linear correlation with key features in regions of deviation—a hyperbolic tangent ($tanh$) switching function is adopted as the foundational modeling structure. As defined in Eq. (6), this formulation utilizes an independent variable m alongside two adjustable parameters. Here, c serves as a threshold that triggers the switch when m exceeds its value, shifting the output to a specific magnitude A, while maintaining a value of 1 elsewhere.

$$\beta(m) = 1.0 + 0.5 \cdot \left(1.0 + \tanh\left(m - c\right)\right) \cdot (A - 1.0). \qquad (6)$$

To ensure compatibility with the function's operational domain, the input features undergo a scaling process to produce $\widehat{Re_\Omega}$ and $\widehat{Re_k}$:

$$Re_\Omega = Re_\Omega \cdot 10^{-4}, Re_k = Re_k \cdot 10^{-4}. \qquad (7)$$

Furthermore, a composite feature $\widehat{Re^*}$ is constructed via a linear combination of these scaled variables, where α_1 acts as the weighting coefficient:

$$Re^* = Re_\Omega + \alpha_1 \cdot Re_k. \quad (8)$$

The hierarchical decision logic that dictates the spatial β correction is illustrated in Figure 4. This multilevel classification scheme is governed by a set of tunable coefficients $\alpha_{2\sim6}$, which function as activation thresholds for the input features ($\widehat{Re_\Omega}, \widehat{Re_k}$, and $\widehat{Re^*}$) and define the magnitude of the correction. The framework employs a primary switch to restrict modifications strictly to the shear layer, while a secondary logical branch distinguishes between the upstream and downstream sectors. This architecture enables the model to effectively suppress eddy viscosity ($\beta < 1$) in the upstream portion of the flow and amplify it ($\beta > 1$) further downstream. The final mathematical form of the model is presented as follows:

$$\begin{aligned}\beta &= 1.0 + 0.5\cdot\left(1.0+\tanh\left(Re_\Omega - \alpha_6\right)\right)\cdot\left(\alpha_5\cdot\beta_1 - 1.0\right),\\ \beta_1 &= 1.0 - \max\left(0.5\cdot\left(1.0-\tanh\left(Re_k-\alpha_3\right)\right), 0.5\cdot\left(1.0+\tanh\left(Re^*-\alpha_4\right)\right)\right)\cdot\left(1.0-\alpha_2\right).\end{aligned} \tag{9}$$

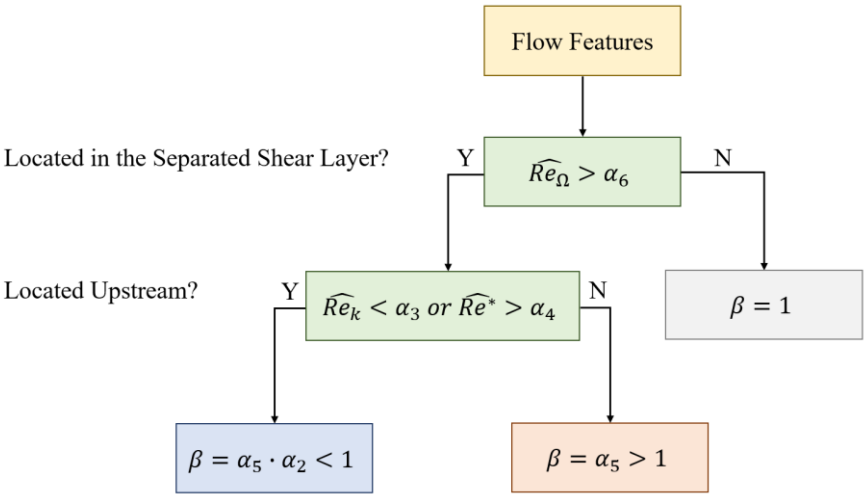
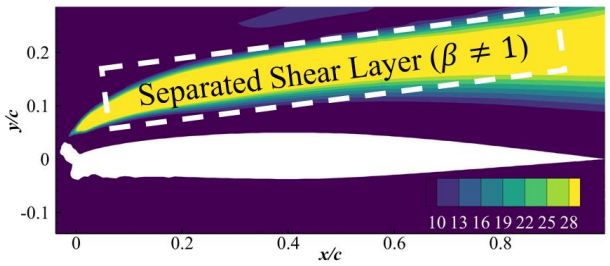


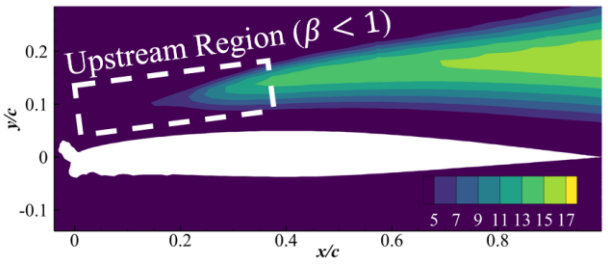
Figure 4 - Schematic of the decision logic for β.

Following the implementation of the β expression within the CFD solver, a CFD-in-loop optimization strategy was executed using a Genetic Algorithm (GA). In this setup, the six undetermined coefficients served as design variables, and the optimization objective was to minimize the sum of squared errors between the predicted and experimental C_L and C_D for the GLC305-944 airfoil at angles of attack $4.14°$ and $6.17°$. The GA process utilized Latin Hypercube Sampling to generate an initial population of 12 individuals, which then evolved over 50 generations. Upon reaching convergence, a Pareto-optimal individual was selected to balance the model's performance across the multiple flow conditions. The final calibrated parameters were determined as follows: $\alpha_1 = -1.04, \alpha_2 = 0.0163, \alpha_3 = 6.51, \alpha_4 = 48.8, \alpha_5 = 3.13, \alpha_6 = 11.7$.

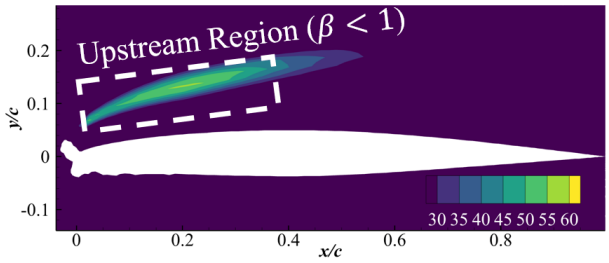
The spatial characteristics of the input features $\widehat{Re_\Omega}$, $\widehat{Re_k}$, and $\widehat{Re^*}$ are visualized in Figure 5. The vorticity-based Reynolds number $\widehat{Re_\Omega}$ spans the full extent of the separated shear layer, making it an ideal candidate for the model's primary activation switch. A key advantage of this feature is the integration of the wall distance d in its formulation, which ensures that even in regions of high shear within the attached boundary layer, the value remains below the activation limit. Consequently, the correction is strictly confined to separated flow regimes. In contrast, the buildup of turbulent kinetic energy exhibits a spatial delay relative to the initiation of the shear layer. As a result, $\widehat{Re_k}$ is primarily concentrated in the downstream section, providing a robust mechanism for distinguishing the later stages of the shear layer from its origin. By leveraging a linear combination of these two variables, the composite feature $\widehat{Re^*}$ is specifically constructed to peak in the upstream region. This provides a precise indicator for identifying the nascent stages of turbulence, thereby facilitating the targeted suppression of eddy viscosity required to rectify the inherent overprediction errors of the baseline SA model. By capturing the unique physical characteristics of these distinct zones, the model successfully implements the necessary corrections for iced airfoil flows, which are characterized by intricate multi-mechanism physics.



(a) $\widehat{Re_\Omega}$.



(b) $\widehat{Re_k}$.



(c) $\widehat{Re^*}$.

Figure 5 - Distribution of features on the GLC305-944 iced airfoil.

4. Model Application

4.1 GLC305-944 Iced Airfoil

The β model with optimized parameters was integrated into the CFD solver. Computations were performed for the GLC305-944 airfoil under $Ma = 0.12,\ Re = 3.5 \times 10^6, \alpha = 6.17°$ condition, yielding the C_P distributions shown in Figure 6. It is evident that the corrected SA model yields a substantial improvement in predicting the surface pressure over the baseline SA model, particularly in capturing the characteristic pressure plateau associated with the post-ice separation bubble. While the baseline SA model typically struggles to resolve the reattachment point on the suction side, the corrected SA model results closely align with both the field inversion data and experimental measurements. This high degree of agreement confirms that the proposed correction model successfully replicates the physical pressure distribution inferred from inversion, effectively rectifying the pressure plateau level that is typically mispredicted by the SA model.

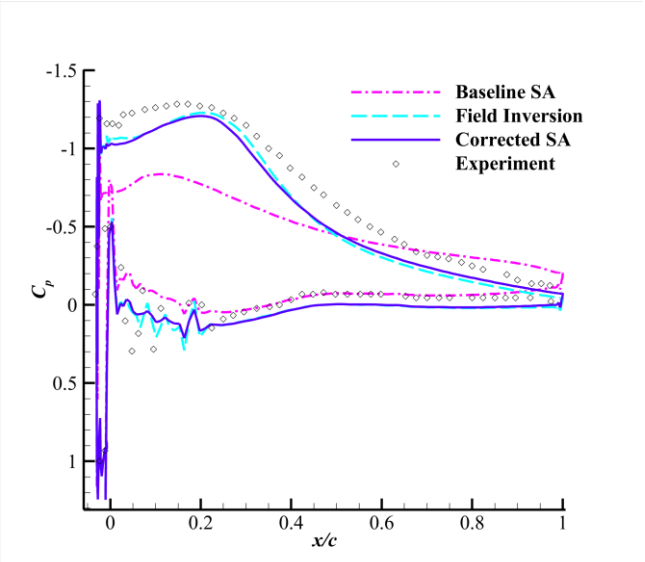
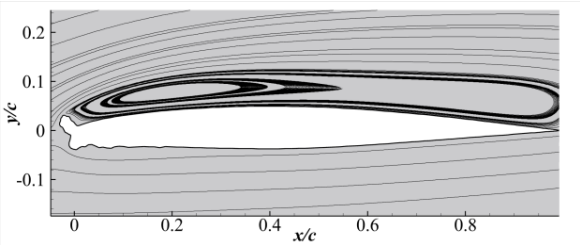
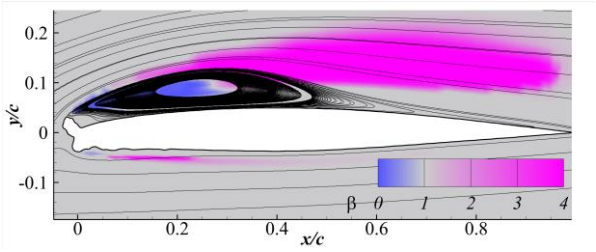


Figure 6 - C_P for the GLC305-944 airfoil.

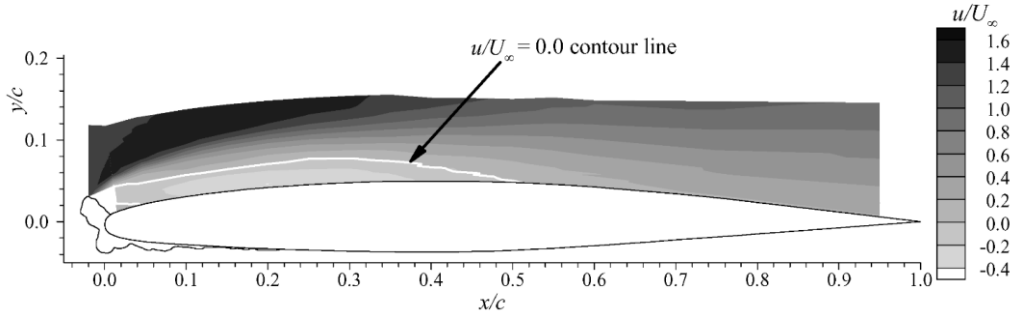
The substantial improvement in surface pressure distributions is intrinsically linked to the accurate reconstruction of the separation topology. Figure 7(b) illustrates the flow field predicted by the corrected SA model alongside the spatial distribution of the correction factor β. The model effectively modulates the eddy viscosity production term by applying suppression in the upstream portion of the shear layer while introducing amplification downstream. This spatial variation directly mirrors the physical mechanisms required to counteract the inherent discrepancies of the baseline SA model. As a result, when compared to the baseline SA results in Figure 7(a), the corrected SA model yields markedly improved predictions regarding the length, size, and overall morphology of the post-ice separation bubble. These refinements bring the simulated flow structures into close alignment with the experimental observations shown in Figure 7(c), demonstrating the model's capability to accurately reconstruct complex physics.



(a) Baseline SA



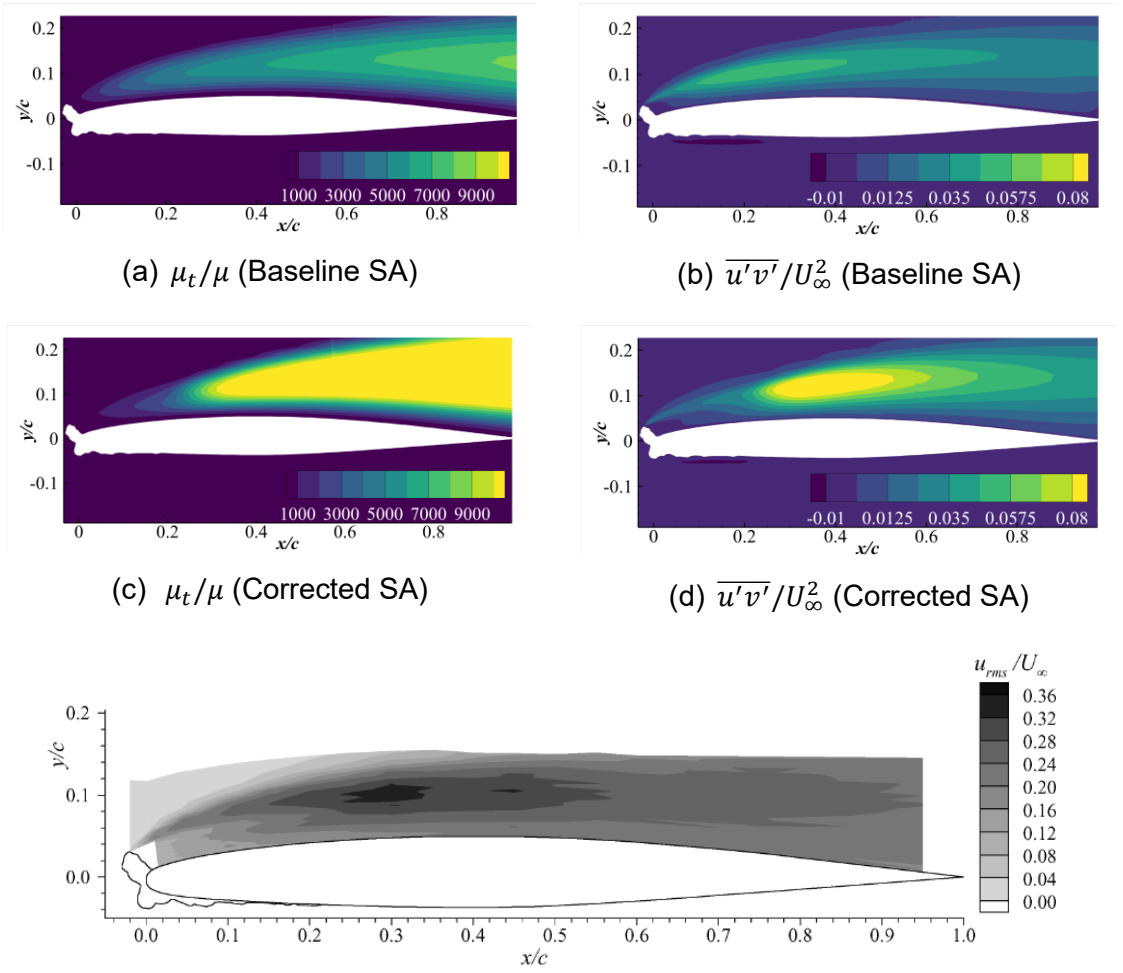
(b) Corrected SA



(c) Experiment[15]

Figure 7 - Flowfield for the GLC305-944 airfoil with experimental data for reference.

The distributions of the dimensionless eddy viscosity μ_t/μ and the Reynolds stress component $\overline{u'v'}/U_\infty^2$ are compared before and after the correction in Figure 8. The spatial modifications introduced to the production term are directly manifested in the eddy viscosity field: production is suppressed in the upstream shear-layer region, where turbulence is still developing, and significantly enhanced further downstream. The corresponding distribution of $\overline{u'v'}/U_\infty^2$, which represents the dominant Reynolds stress within the shear layer, follows a similar trend, providing further evidence of the corrective effects. When evaluated against the experimental u_{rms}/U_∞ data in Figure 8(e), the corrected SA model demonstrates a substantial improvement in predictive accuracy. Specifically, the model yields result that closely match the experimental data in both the overall profile shape and the precise location of the peak fluctuations, validating the effectiveness of the physics-driven classification modeling approach.



(a) μ_t/μ (Baseline SA)

(b) $\overline{u'v'}/U_\infty^2$ (Baseline SA)

(c) μ_t/μ (Corrected SA)

(d) $\overline{u'v'}/U_\infty^2$ (Corrected SA)

(e) u_{rms}/U_∞ (Experiment) [15]

Figure 8 - Comparison of μ_t/μ and $\overline{u'v'}/U_\infty^2$ for the GLC305-944 airfoil with u_{rms}/u_∞ from the experiment.

Furthermore, the model's performance was evaluated across a comprehensive range of angles of attack, with the resulting C_L curves presented in Figure 9. The results indicate that the corrected model yields consistent improvements in predictive fidelity across the entire polar. Specifically, the model effectively rectifies the underprediction of the lift-line slope in the linear region and provides a significantly more realistic estimation of the stall angle. At high angles of attack, where strong unsteady effects are present, the force coefficients were obtained by averaging the oscillating results, and these predictions are denoted by dashed lines. Given that the model parameters were optimized using data from only two specific conditions ($\alpha = 4.14°$ and $6.17°$), the close agreement with experimental data across the entire polar curve provides compelling evidence of the model's generalization capability. This demonstrates that the physics-driven features effectively capture the underlying mechanisms of iced-airfoil flows, allowing the model to remain robust beyond its training envelope.

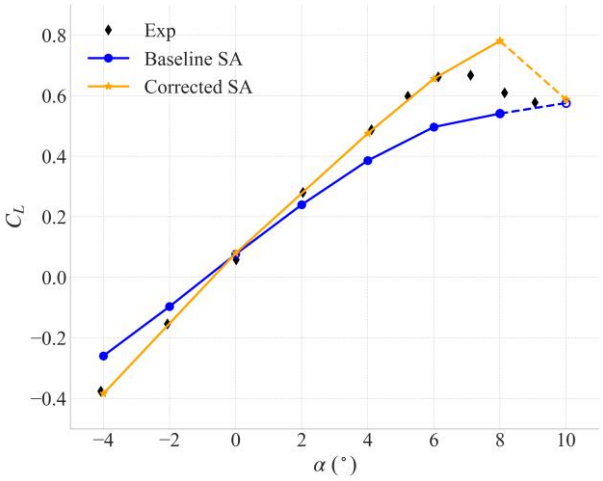
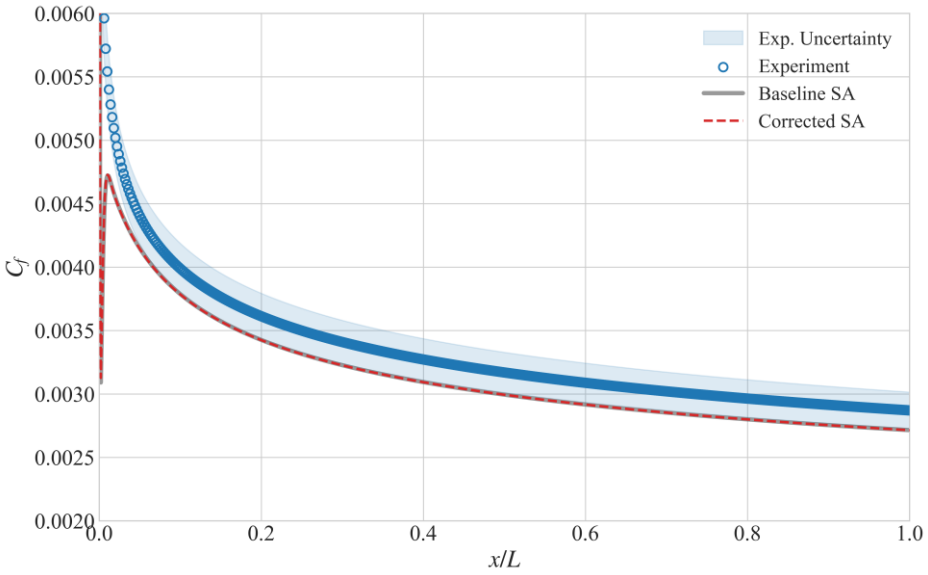


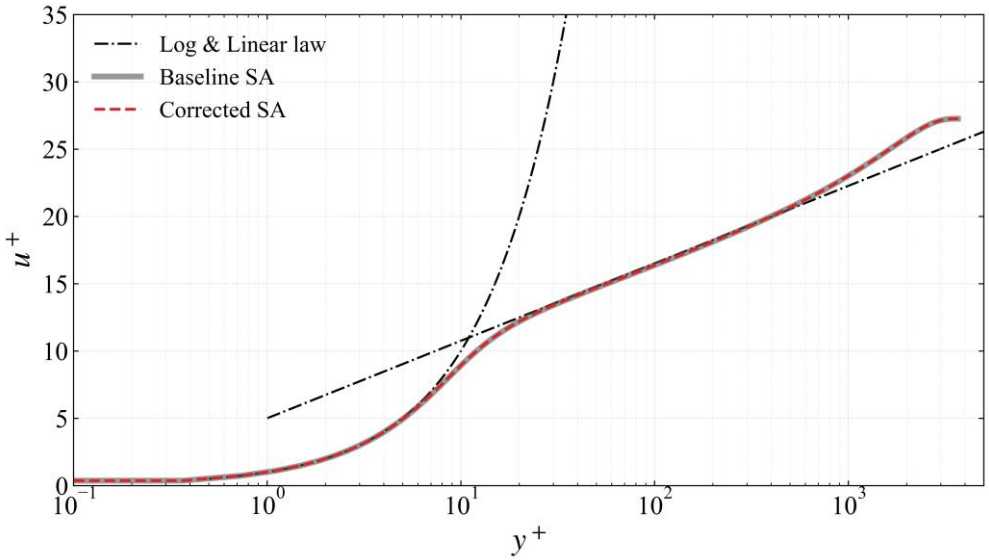
Figure 9 – Comparison of the C_L curve for the GLC305-944 airfoil using the corrected SA model

4.2 Zero-Pressure-Gradient Flat-Plate

To ensure that the introduced corrections do not inadvertently degrade the model's accuracy in canonical attached flows, the corrected SA model was evaluated using a zero-pressure-gradient (ZPG) flat-plate benchmark. Following the experimental setup of reference [17], the freestream conditions were defined by $Ma = 0.2$ and a Reynolds number per unit length of $Re_L = 5 \times 10^6$. Figure 10(a) compares the skin friction coefficient C_f distributions obtained from both the baseline SA and the corrected SA models. The results are virtually indistinguishable, confirming that the modification term remains inactive in the attached boundary layer. This consistency is further evidenced by the boundary layer velocity profiles at $Re_x = 5 \times 10^6$ shown in Figure 10(b). The corrected SA model precisely recovers the baseline velocity distribution, strictly adhering to the linear and logarithmic laws of the attached flow. These results validate the "shielding" capability of the Re_Ω feature discussed in Section 3. This feature exhibits superior diagnostic performance by enabling the model to accurately identify and deactivate the correction within attached boundary layers. Consequently, the corrected SA model preserves the accuracy of the original SA model in canonical simple flows, ensuring that its predictive integrity for standard wall-bounded flows remains uncompromised.



(a) C_f



(b) Velocity profiles

Figure 10 – Results on the ZPG flat plate.

5. Conclusion

The present study developed an augmented version of the SA model within the FI-PDCM framework to address the "dual error mechanism" in iced-airfoil flows. By integrating physical insights with data-driven correlation analysis, two key local features Re_Ω and Re_k were identified to effectively decouple the opposing requirements for eddy viscosity suppression and amplification. Results on the GLC305-944 iced airfoil demonstrate that the model accurately reconstructs the separation bubble physics, rectifies the surface pressure plateau, and improves the lift-line slope and stall angle predictions. Furthermore, validation on a ZPG flat plate confirms that the model's capability preserves the accuracy of the baseline SA model in canonical attached flows. Future work will focus on assessing the model's robustness and generalizability across diverse ice configurations, with the ultimate goal of ensuring its industrial applicability and practical engineering value.

6. Copyright Statement

The authors confirm that they, and/or their company or organization, hold copyright on all of the original material included in this paper. The authors also confirm that they have obtained permission, from the copyright holder of any third party material included in this paper, to publish it as part of their paper. The authors confirm that they give permission, or have obtained permission from the copyright holder of this paper, for the publication and distribution of this paper as part of the ICAS proceedings or as individual off-prints from the proceedings.

7. References

[1] Singh, A. P., and Duraisamy, K., "Using Field Inversion to Quantify Functional Errors in Turbulence Closures," *Physics of Fluids*, Vol. 28, No. 4, 2016, p. 045110.

[2] He, Z., Wu, C., and Zhang, Y., "A Field Inversion and Symbolic Regression Enhanced Spalart–Allmaras Model for Airfoil Stall Prediction," Physics of Fluids, Vol. 36, No. 6, 2024, p. 065111.

[3] Wu, C., Zhang, S., and Zhang, Y., "Development of a Generalizable Data-Driven Turbulence Model: Conditioned Field Inversion and Symbolic Regression," AIAA Journal, Vol. 63, No. 2, 2024, pp. 1–20.

[4] Duraisamy, K., Spalart, P. R., and Rumsey, C. L., "Status, Emerging Ideas and Future Directions of Turbulence Modeling Research in Aeronautics," NASA TM 2017-219682, 2017.

[5] Yan, C., Li, H., Zhang, Y., and Chen, H., "Data-Driven Turbulence Modeling in Separated Flows Considering Physical Mechanism Analysis," International Journal of Heat and Fluid Flow, Vol. 96, Aug. 2022, Paper 109004.

[6] Xiao, M., and Zhang, Y., "Improved Prediction of Flow Around Airfoil Accreted with Horn or Ridge Ice," AIAA Journal, Vol. 59, No. 6, 2021, pp. 2318–2327.

[7] Spalart, P., and Allmaras, S., "A One-Equation Turbulence Model for Aerodynamic Flows," presented at

the 30th aerospace sciences meeting and exhibit, 1992.
[8] Elliott, J., and Peraire, J., “Practical Three-Dimensional Aerodynamic Design and Optimization Using Unstructured Meshes,” *AIAA Journal*, Vol. 35, No. 9, 1997, pp. 1479–1485.
[9] Duffy, A. C., “An Introduction to Gradient Computation by the Discrete Adjoint Method,” TR, 2009
[10] Kenway, G. K., Mader, C. A., He, P., and Martins, J. R., “Effective Adjoint Approaches for Computational Fluid Dynamics,” *Progress in Aerospace Sciences*, Vol. 110, 2019, p. 100542.
[11] Srivastava, V., Rumsey, C., Coleman, G., and Wang, L., “Augmenting RANS Turbulence Models Guided by Field Inversion and Machine Learning,” NASA/TM-20240012512, 2024.
[12] Holland, J. R., Baeder, J. D., and Duraisamy, K., “Field Inversion and Machine Learning with Embedded Neural Networks: PhysicsConsistent Neural Network Training,” AIAA Aviation 2019 Forum, AIAA Paper 2019-3200, 2019.
[13] Storn, R., and Price, K., “Differential Evolution–A Simple and Efficient Heuristic for Global Optimization over Continuous Spaces,” Journal of Global Optimization, Vol. 11, No. 4, 1997, pp. 341–359.
[14] Deng, K., and Chen, H., “A Hybrid Aerodynamic Optimization Algorithm Based on Differential Evolution and RBF Response Surface,” 17th AIAA/ISSMO Multidisciplinary Analysis and Optimization Conference, AIAA Paper 2016-3671, 2016.
[15] Broeren, A. P., Bragg, M. B., and Addy, H. E., “Flowfield Measurements about an Airfoil with Leading-Edge Ice Shapes,” *Journal of Aircraft*, Vol. 43, No. 4, 2006, pp. 1226–1234.
[16] Li, H., Zhang, Y., and Chen, H., “Aerodynamic Prediction of Iced Airfoils Based on Modified Three-[Equation Turbulence Model,” *AIAA Journal*, Vol. 58, No. 9, 2020, pp. 3863–3876.
[17] Wieghardt, K., and Tillmann, W., “On the Turbulent Friction Layer for Rising Pressure,” NACA TM 1314, 1951.